Check for updates

ORIGINAL ARTICLE

Characterisation of the anisotropic response of wire and arc additively manufactured stainless steel

Nicolas Hadjipantelis[1,2,3], Ben Weber[2], Leroy Gardner[2,3]

Correspondence

Dr. Nicolas Hadjipantelis
University of Cyprus
Department of Civil and Environmental Engineering
1 Panepistimiou Avenue
2109 Nicosia, Cyprus
Email: hadjipantelis.nicolas@ucy.ac.cy

Affiliations

[1]Department of Civil and Environmental Engineering, University of Cyprus, Nicosia, Cyprus.
[2]Department of Civil and Environmental Engineering, Imperial College London, London, United Kingdom.
[3]Data-Centric Engineering Programme, the Alan Turing Institute, London, United Kingdom.

Abstract

In contrast to conventional structural steel and stainless steel, wire and arc additively manufactured (WAAM) material can exhibit a strongly anisotropic response. To investigate the degree of anisotropy in WAAM sheet material, data obtained from tensile tests on machined and as-built stainless steel coupons are utilised. The WAAM material was tested in three different loading directions relative to the deposition direction and the response was captured using digital image correlation; a summary of the key results is presented. In the elastic range, the observed mechanical response is characterised using an orthotropic plane stress material model, which requires the definition of two Young's moduli, the Poisson's ratio and the shear modulus. Good agreement between the test results and the theoretical predictions based on the orthotropic material model is demonstrated. In the inelastic range, to describe the anisotropic yielding of the material, the well-known Hill's criterion utilising the 0.2% proof stresses is employed. Overall, the elastic and inelastic properties of the studied material are shown to vary significantly with the direction of loading.

Keywords

Digital image correlation, Material anisotropy, Mechanical response, Orthotropic material modelling, Stainless steel, Tensile coupon tests, Wire and arc additive manufacturing, 3D printing

1 Introduction

As seen in the aerospace, automotive and healthcare industries [1-4], the introduction of digitally-enabled techniques, such as 3D printing, is projected to also have a transformative effect in the construction industry [5-7]. Wire and arc additive manufacturing (WAAM) [8] is a metal 3D printing technique that employs a robotic arm, such as that shown in Figure 1, to print metallic components of any desired geometry and size [9,10] in a layer upon layer fashion. The revolutionary aspect of WAAM is that it allows the production of bespoke structural components that are not technologically or economically feasible with conventional formative (e.g. hot-rolling) or subtractive (e.g. milling) shaping techniques [6,7]. By placing the material where it is most needed, WAAM can lead to greater structural efficiency, reduced material use and reduced waste. For example, the Dutch company MX3D [11] has reverse-engineered, topologically optimised and printed a replacement part for an ABB industrial robot, shown in Figure 2, achieving over 50% weight reductions in comparison with the original part [11].

Significant barriers to the wider use of additive manufacturing in construction include the lack of standardisation for manufacturing, quality assurance and design [1,7]. These barriers relate, to a large extent, to the scarcity of test data on the mechanical properties of additively manufactured materials [12,13].
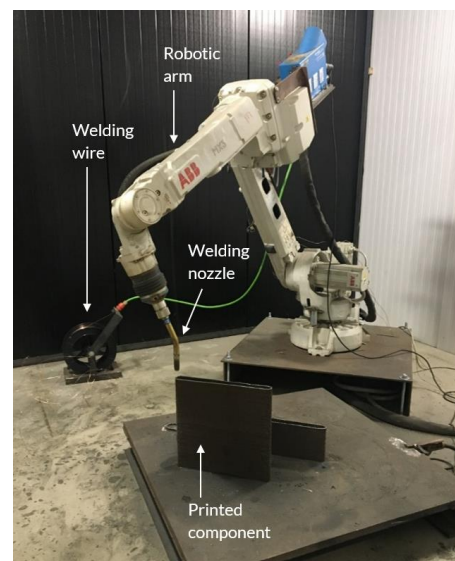

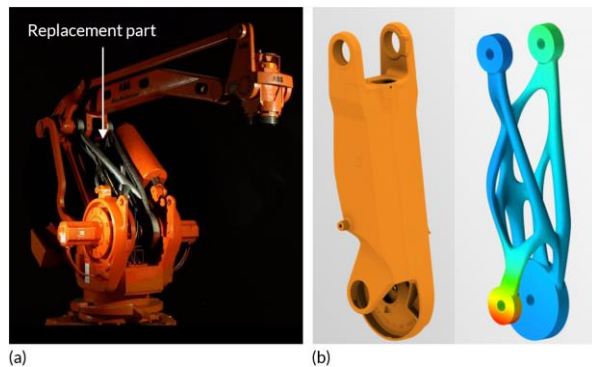**Figure 1** Robotic arm used in WAAM. Source: MX3D [11].

Figure 2 (a) ABB robot with WAAM replacement part attached. (b) Original (left) and topologically optimised (right) geometries of the part. Source: MX3D [11].

In light of this, there has recently been a growing number of research groups investigating the microstructural and mechanical properties of different WAAM materials, including low–carbon steels [14,15] and various stainless steel alloys [16-20]. All the aforementioned studies have revealed a degree of anisotropy in the behaviour of WAAM material, i.e. its mechanical response is influenced by the direction of loading relative to the deposition direction. The material anisotropy is inherent to the manufacturing process, which, owing to the deposition of welding material in layers, results in solidification under a distinct thermal gradient [20]. In contrast to conventional structural steel and stainless steel, which generally behave isotropically (i.e. mechanical properties are independent of orientation at any given point in the material), anisotropy in additively manufactured materials can be significant [21].

In this paper, the findings of an experimental study into the degree of material anisotropy in WAAM stainless steel are presented and analysed. Following a description of the experimental programme, the elastic mechanical response of the WAAM material is characterised using an orthotropic plane stress model requiring the determination of four independent elastic constants. Subsequently, the inelastic mechanical response is described by means of the Hill's criterion and the 0.2% proof stresses. Finally, the results are discussed and conclusions are drawn.

2 Experimental study

The experimental data utilised in the present paper was obtained by means of tensile coupon testing which was conducted in compliance with EN ISO 6892-1 [45] in the Structures Laboratory of the Department of Civil and Environmental Engineering at Imperial College London, as described by Kyvelou et al. (2020).

2.1 Test specimens

The test coupons were extracted from WAAM plates manufactured by the Dutch company MX3D [11] using Grade 308LSi austenitic stainless steel. Two types of tensile coupons, namely as-built and machined, were tested. The as-built coupons were cut directly from the WAAM plates. In total, 37 as-built coupons were tested – 17 with a nominal thickness of 3.5 mm and 20 with a nominal thickness of 8.0 mm. The machined coupons were fashioned from as-built material of 8.0 mm nominal thickness using an end mill, thus removing the inherently undulating surface of the as-built material and resulting in prismatic coupons (within the parallel length) with uniform thickness, as shown in Figure 3. In this manner, the (weakening) effect of the geometric undulations was eliminated, and thus the true characteristics of the underlying material could be studied. In total, 12 machined coupons were tested. To investigate anisotropy in WAAM material, the coupons were extracted and tested under ten-

sion at three different orientations relative to the deposition direction, namely at an angle $\theta = \{0°, 45°, 90°\}$ as defined in Figure 4.

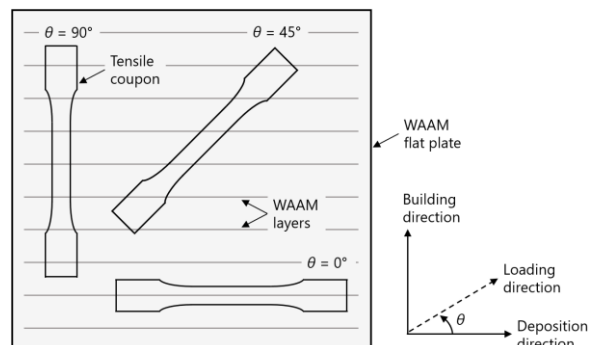**Figure 3** (a) Extracted as-built and (b) machined coupons [20].

Figure 4 Orientations of the coupons relative to deposition direction.

2.2 Test setup and data acquisition

A 250 kN Instron 8802 testing machine was employed to apply monotonic uniaxial loading to the coupons until fracture using strain control. The applied loading was measured by a load cell within the actuator. Prior to testing, the surface geometry of the as-built coupons was registered by means of 3D laser scanning to capture the geometric undulations, shown in Figure 3(a), that are inherent to the WAAM process. A four-camera LaVision [46] digital image correlation (DIC) system, shown in Figure 5, in conjunction with the DaVis software [46], was utilised to measure the full surface strain field during testing by capturing images from both sides of the coupons at a frequency of 1 Hz. This approach played a critical role in the current study since, as shown below, the strain field across WAAM elements is highly non-uniform.

The average axial stress level was obtained by dividing the measured tensile load by the mean cross-sectional area over the parallel length of the coupons, as determined using the laser scanning data [20]. The average longitudinal and transverse strains were obtained directly using the DaVis software by considering a rectangular area over the full parallel length, as shown in Figure 6; this was performed for both sides of the coupon and an average was then taken. The obtained stress–strain data were: (i) centred to the origin to account for any preload effects, (ii) smoothed using a moving average filter with a span of 15 data points, and (iii) distributed evenly along the stress axis. The mechanical properties of each coupon were subsequently determined as described below.
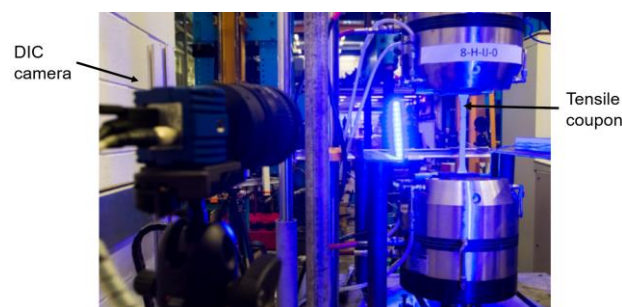

Figure 5 DIC system used in the tensile coupon testing [20].

2.3 Test results

2.3.1 Origin of material anisotropy

The inherent anisotropy in WAAM material is evident in Figure 6, where the longitudinal surface strain fields of the $\theta = \{0°, 45°, 90°\}$ machined coupons are shown. As concluded by Kyvelou et al. (2020) and Wang et al. (2019), who employed electron backscatter diffraction to explore the internal microstructure of WAAM material, the anisotropy originates from the preferential crystallographic alignment along the highest thermal gradient (i.e. along the building direction, as defined in Figure 4) during the rapid solidification of the melted material. Consequently, the mechanical behaviour of the material can become highly dependent on the direction of loading. A similar conclusion was reached by Laghi et al. (2020) using 3D digital microscopy.
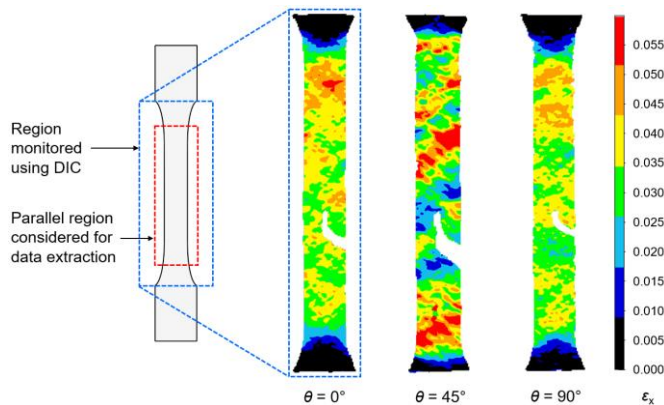
Figure 6 Example of the typical longitudinal surface strain fields of machined coupons at 3.5% average longitudinal strain.

2.3.2 Anisotropy in stress–strain responses

The stress–strain (σ–ε) responses of the as-built and machined coupons are shown in Figures 7 and 8, respectively, where the longitudinal stress is plotted in terms of both the average longitudinal ε_x and transverse ε_y strains; positive strain values indicate material elongation while negative values indicate material contraction. The average Young's moduli E_x, 0.2% proof stresses $\sigma_{0.2}$, ultimate stresses σ_u and ultimate longitudinal $\varepsilon_{x,u}$ and transverse $\varepsilon_{y,u}$ strains of the as-built 3.5 mm, as-built 8.0 mm and machined coupons are listed in Tables 1, 2 and 3, respectively. The material properties of the as-built coupons are reported as being 'effective', owing to the influence of the geometric variability on their mechanical response [20]. Additional properties, including the 1.0% proof stresses and fracture strains can be found in [20], where the process of determining the aforementioned properties is described in detail.

Overall, it can be concluded that there is a high degree of anisotropy in WAAM material, since the Young's modulus, strength and ductility are highly dependent on the direction of loading relative to the deposition direction. Generally, the responses of the as-built and machined coupons followed similar trends, with all coupons demonstrating ductile behaviour (except one as-built 8.0 mm $\theta = 90°$ specimen that had a local lack of fusion [20]). All effective mechanical properties of the as-built coupons were lower than those of the machined coupons (except from $\varepsilon_{y,u,eff}$ of the 3.5 mm $\theta = 0°$ coupons, and $\varepsilon_{x,u,eff}$ and $\varepsilon_{y,u,eff}$ of the 8.0 mm $\theta = 0°$ coupons). This is attributed to the negative impact of the geometric undulations [20, 22], which induce eccentricities and thus bending during tensile loading, on the material response. The $\theta = 45°$ and $\theta = 90°$ coupons demonstrated, respectively, the highest and lowest Young's modulus, strength and ductility (longitudinally). Comparing the average properties of the different coupon sets, the following conclusions can be drawn:
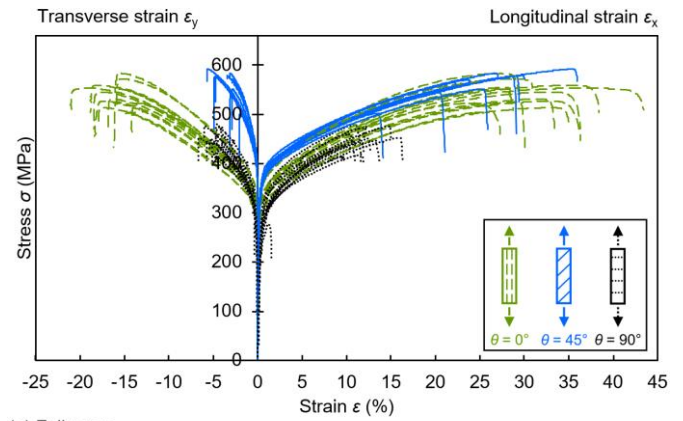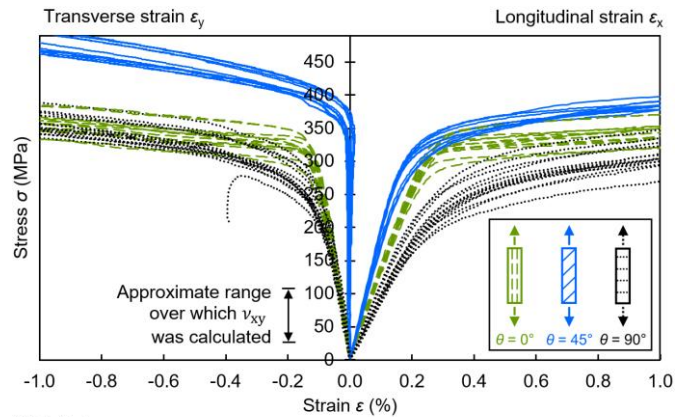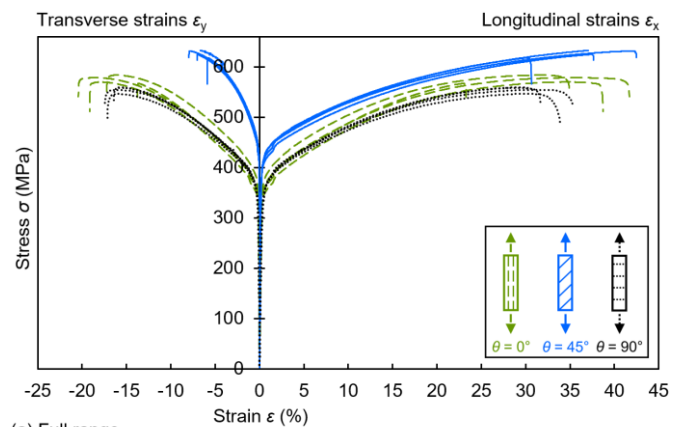
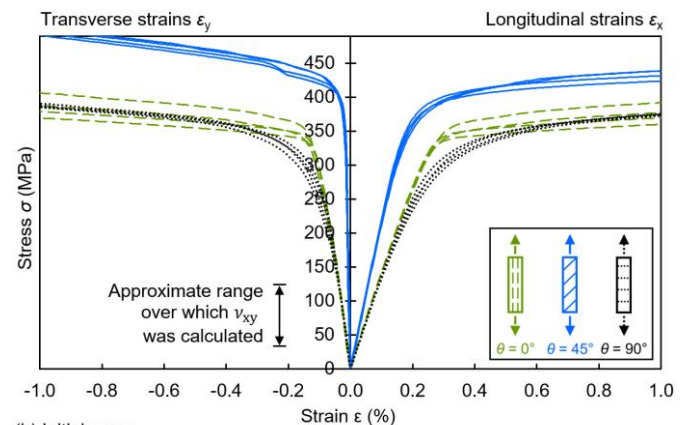**Figure 7** Stress–strain responses of the as-built specimens over (a) the full range and (b) the initial range.

Figure 8 Stress–strain responses of the machined specimens over (a) the full range and (b) the initial range.

As-built 3.5 mm coupons: The $\theta = 45°$ coupons achieved effective Young's modulus, 0.2% proof stress, ultimate stress and ultimate longitudinal strain values that were 114%, 32%, 27% and 114%, respectively, higher than those of the $\theta = 90°$ coupons. The $\theta = 0°$ coupons achieved similar values to the $\theta = 45°$ coupons, except from the effective Young's modulus which was 42% lower. The effective ultimate transverse strain of the $\theta = 45°$ coupons was 32% and 80% lower than that of the $\theta = 90°$ and $\theta = 0°$ coupons, respectively.

As-built 8.0 mm coupons: The effective Young's modulus, 0.2% proof stress, ultimate stress and ultimate longitudinal strain values of the $\theta = 45°$ coupons were, respectively, 84%, 30%, 32% and 148% higher than those of the $\theta = 90°$ coupons. Similar values were achieved by the $\theta = 0°$ coupons, except for a 47% lower effective Young's modulus and a 22% higher effective ultimate longitudinal strain. In the transverse direction, the $\theta = 45°$ coupons demonstrated 22% and 78% lower effective ultimate strains than the $\theta = 90°$ and $\theta = 0°$ coupons, respectively.

Machined coupons: The Young's modulus of the $\theta = 45°$ coupons was more than 50% higher than that of the $\theta = 0°$ and $\theta = 90°$ coupons, which achieved a similar value between them. The $\theta = 45°$ coupons achieved 20% and 13% higher 0.2% proof stress and ultimate stress values, respectively, than the $\theta = 90°$ coupons; relative to the $\theta = 0°$ coupons, this difference is slightly lower. The ultimate longitudinal strain of the $\theta = 45°$ coupons was approximately 20% higher than that of the $\theta = 0°$ and $\theta = 90°$ coupons, which achieved a similar value between them. Transversely, the $\theta = 45°$ coupons demonstrated 67% lower ultimate strain than the $\theta = 0°$ and $\theta = 90°$ coupons.

Table 1 Average effective mechanical properties of the as-built 3.5 mm coupons.

θ	E_{eff}	$\sigma_{0.2,eff}$	$\sigma_{u,eff}$	$\varepsilon_{x,u,eff}$	$\varepsilon_{y,u,eff}$
(°)	(GPa)	(MPa)	(MPa)	(%)	(%)
0	135.9	333	553	27.3	-15.0
45	192.6	344	570	25.5	-3.0
90	90.2	261	448	11.9	-4.4

Table 2 Average effective mechanical properties of the as-built 8.0 mm coupons.

θ	E_{eff}	$\sigma_{0.2,eff}$	$\sigma_{u,eff}$	$\varepsilon_{x,u,eff}$	$\varepsilon_{y,u,eff}$
(°)	(GPa)	(MPa)	(MPa)	(%)	(%)
0	137.1	325	535	32.5	-17.3
45	201.2	351	559	25.5	-3.8
90	109.1	271	423	10.3	-4.9

Table 3 Average mechanical properties of the machined coupons.

θ	E	$\sigma_{0.2}$	σ_u	$\varepsilon_{x,u}$	$\varepsilon_{y,u}$
(°)	(GPa)	(MPa)	(MPa)	(%)	(%)
0	143.3	356	575	30.7	-14.7
45	219.5	407	626	36.4	-4.8
90	139.6	338	554	29.7	-14.5

3 Elastic mechanical response

3.1 Adopted material model

WAAM material is heterogeneous since it exhibits nonuniform distributions of properties, as illustrated in Figure 6. In the current work, as discussed in Section 2.3.2, the constitutive response of WAAM material is examined by considering its average macroscopic properties; hence, it is effectively treated as being homogeneous, with its mechanical properties being uniformly distributed and independent of location within the specimens.

The coordinate systems adopted in this work are illustrated in Figure 9. The 1– and 2– directions in the principal material coordinate system (1–2–3) correspond to the deposition and building directions, respectively, as shown in Figure 4. The principal material coordinate system is oriented at an angle θ relative to the Cartesian coordinate system (x–y–z), with the x–, y– and z–directions corresponding to the longitudinal (i.e. loading), transverse and out-of-plane directions, respectively. Thus, the angle θ indicates the loading direction with respect to the deposition direction. According to the adopted coordinate systems, the deposition direction of the $\theta = 0°$ and $\theta = 90°$ coupons is aligned with the x– and y– Cartesian axes, respectively, as shown in Figure 10. In the case of $\theta = 45°$, owing to the misalignment between the principal and Cartesian axes, the coupons are subjected to so-called 'off-axis loading' [23], which takes place when $\theta \neq 0°$ or $\theta \neq 90°$.
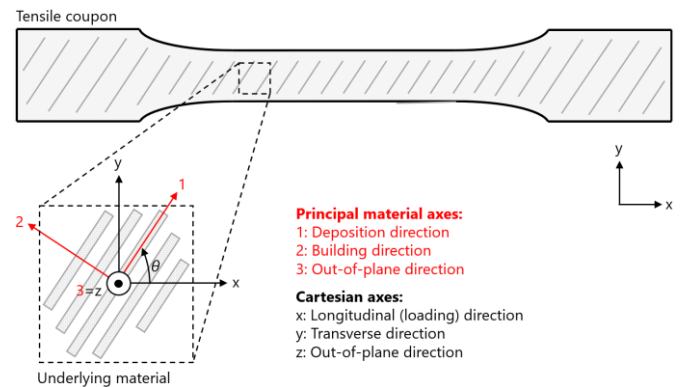

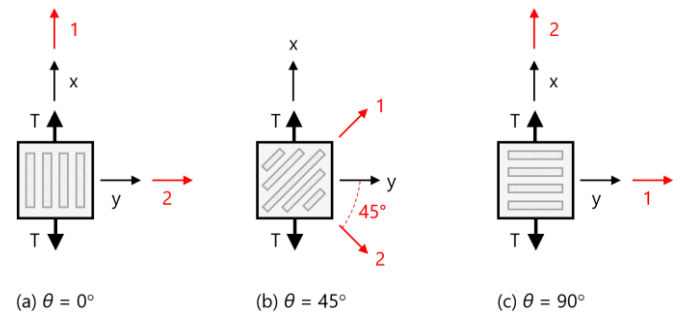**Figure 9** Adopted coordinate systems (for an arbitrary angle θ).

(a) $\theta = 0°$ (b) $\theta = 45°$ (c) $\theta = 90°$

Figure 10 Material orientation in the $\theta = \{0°, 45°, 90°\}$ coupons where T denotes the applied tensile load.

Owing to their thin-walled geometry, the WAAM elements studied herein can be assumed to be under plane stress conditions. Furthermore, as evident from the test results presented in Section 2.3, WAAM material demonstrates different mechanical properties in the two orthogonal in-plane directions. Hence, an orthotropic plane stress material model is employed. Orthotropic materials are a subset of anisotropic materials, having three mutually orthogonal planes of property symmetry and, at any given point, having different properties in three mutually orthogonal directions [23]. The same models have been adopted by Bruggi et al. (2021) and Dodwell et al. (2021); the special case of transverse isotropy has been assumed in the latter.

3.2 Theoretical basis

3.2.1 Orthotropic plane stress material model

Compared to fully anisotropic material models, which require 21 independent elastic constants, orthotropic models require only 9, namely three Young's moduli, three Poisson's ratios and three shear moduli. In the adopted model, plane stress conditions (within the 1–2 plane), in conjunction with the reciprocal equation:

$$\frac{\nu_{12}}{E_1} = \frac{\nu_{21}}{E_2} ,$$ (1)

reduce the number of independent constants to 4, namely two Young's moduli E_1 and E_2 in the 1– and 2–directions, respectively, one Poisson's ratio $\nu_{12} = -\varepsilon_2/\varepsilon_1$ relating the transverse strains to the longitudinal strains when stress is applied in the 1–direction, and one shear modulus G_{12} in the 1–2 plane. The σ–ε relationships with respect to the in-plane (1–2) principal material axes are obtained using the compliance matrix **S** [23, 37]:

$$\mathbf{S} = \begin{bmatrix} 1/E_1 & -\nu_{21}/E_2 & 0 \\ -\nu_{12}/E_1 & 1/E_2 & 0 \\ 0 & 0 & 1/G_{12} \end{bmatrix} ,$$ (2)

such that:

$$\begin{bmatrix} \varepsilon_1 \\ \varepsilon_2 \\ \gamma_{12} \end{bmatrix} = \mathbf{S} \begin{bmatrix} \sigma_1 \\ \sigma_2 \\ \tau_{12} \end{bmatrix} = \begin{bmatrix} 1/E_1 & -\nu_{21}/E_2 & 0 \\ -\nu_{12}/E_1 & 1/E_2 & 0 \\ 0 & 0 & 1/G_{12} \end{bmatrix} \begin{bmatrix} \sigma_1 \\ \sigma_2 \\ \tau_{12} \end{bmatrix} ,$$ (3)

where τ_{12} and γ_{12}, are the shear stress and strain in the 1–2 plane, respectively. Equation (3) is subject to the conditions $E_1, E_2, G_{12} > 0$ and $|\nu_{12}| < \sqrt{E_1/E_2}$ [34].

Constants E_1, E_2 and ν_{12} can be obtained directly through coupon testing. However, to obtain the shear modulus G_{12}, the Young's modulus from one off-axis loading test is also required. For this purpose, off-axis loading tests with $\theta = 45°$, as shown in Figure 10(b), are typically undertaken. In off-axis loading, where orthotropic material is not loaded along its principal material axes, the stresses and strains in the Cartesian coordinate system (i.e. ε_x, ε_y, γ_{xy}, σ_x, σ_y and τ_{xy}) and the four elastic constants in the principal material coordinate system (i.e. E_1, E_2, ν_{12} and G_{12}) can be related using the compliance matrix **S** in conjunction with the transformation matrix **T**:

$$\mathbf{T} = \begin{bmatrix} c^2 & s^2 & 2sc \\ s^2 & c^2 & -2sc \\ -sc & sc & c^2 - s^2 \end{bmatrix} ,$$ (4)

where $c = \cos\theta$ and $s = \sin\theta$, such that:

$$\begin{bmatrix} \varepsilon_x \\ \varepsilon_y \\ \gamma_{xy} \end{bmatrix} = \mathbf{T}^{-1}\mathbf{S}\mathbf{T} \begin{bmatrix} \sigma_x \\ \sigma_y \\ \tau_{xy} \end{bmatrix} ,$$ (5)

where $\mathbf{T}^{-1}$ is the inverse matrix of **T**. In this manner, transformation relationships between the material properties in the Cartesian coordinate system (i.e. E_x, E_y, ν_{xy} and G_{xy}) and the elastic constants in the principal material coordinate system, can be obtained [23], thus:

$$\frac{1}{E_x} = \frac{1}{E_1}c^4 + \left(\frac{1}{G_{12}} - \frac{2\nu_{12}}{E_1}\right)s^2c^2 + \frac{1}{E_2}s^4 ,$$ (6)

$$\frac{1}{E_y} = \frac{1}{E_1}s^4 + \left(\frac{1}{G_{12}} - \frac{2\nu_{12}}{E_1}\right)s^2c^2 + \frac{1}{E_2}c^4 ,$$ (7)

$$\nu_{xy} = E_x\left[\frac{\nu_{12}}{E_1}(s^4 + c^4) - \left(\frac{1}{E_1} + \frac{1}{E_2} - \frac{1}{G_{12}}\right)s^2c^2\right] ,$$ (8)

$$\frac{1}{G_{xy}} = 2\left[\frac{2}{E_1} + \frac{2}{E_2} + \frac{4\nu_{12}}{E_1} - \frac{1}{G_{12}}\right]s^2c^2 + \frac{1}{G_{12}}(s^4 + c^4) .$$ (9)

By rearranging Equation (6), the expression for determining G_{12} by means of off-axis testing [23, 44] can be obtained:

$$G_{12} = \left[\frac{2\nu_{12}}{E_1} + \frac{1}{s^2c^2}\left(\frac{1}{E_x} - \frac{c^4}{E_1} - \frac{s^4}{E_2}\right)\right]^{-1} ,$$ (10)

which, in the case of $\theta = 45°$, as in the current work, becomes:

$$G_{12} = \left[\frac{4}{E_{x,45°}} + \frac{2\nu_{12} - 1}{E_1} - \frac{1}{E_2}\right]^{-1} ,$$ (11)

where $E_{x,45°}$ is the Young's modulus measured in the $\theta = 45°$ tests.

According to Equation (3), in an orthotropic material subjected to stresses only about its principal axes, there is no interaction between normal stresses and shear strains (and vice versa), as illustrated in Figure 11(a). However, in the case of off-axis loading, according to Equation (5), coupling between normal stresses and shear strain occurs; hence, as illustrated in Figure 11(b), both axial and shear deformations develop. This interaction can be represented by means of shear–extension coupling coefficients [23, 24, 27, 43], such as the 'coefficient of mutual influence of the second kind' $\eta_{xy,x}$:

$$\eta_{xy,x} = \frac{\gamma_{xy}}{\varepsilon_x} = E_x\left[\left(\frac{2}{E_1} + \frac{2\nu_{12}}{E_1} - \frac{1}{G_{12}}\right)sc^3 - \left(\frac{2}{E_2} + \frac{2\nu_{12}}{E_1} - \frac{1}{G_{12}}\right)s^3c\right] ,$$ (12)

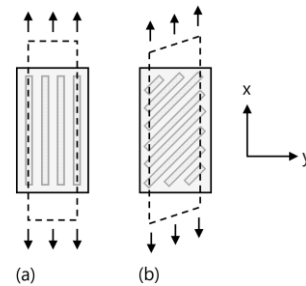which characterises shear strains in the x–y plane due to normal stress in the x–direction.

Figure 11 Illustrations of normal and shear deformations in an orthotropic material when loaded (a) along and (b) at an angle to the principal axes. Adapted from [24].

3.3 Elastic constants

Based on the test results presented in Section 2.3, the four independent elastic constants required to characterise the elastic mechanical response of WAAM elements have been obtained.

The elastic constants reported below can be employed in finite shell element simulations in conjunction with an orthotropic plane stress material model. In the widely used software ABAQUS [28], this can be achieved using the *ELASTIC, TYPE=LAMINA command.

3.3.1 Young's modulus

The average Young's moduli for $\theta = \{0°, 45°, 90°\}$, as determined using the process described in [20], are reported in Tables 4–6, where E_x is the average value obtained directly from the tensile tests. Since the applied stress was along the x–direction, E_y has been taken as the average Young's modulus corresponding to the $\theta = 90°$ tests; hence, with Figure 10 in mind: (i) $E_{x,0°} = E_{y,90°} = E_1$, (ii) $E_{y,0°} = E_{x,90°} = E_2$ and (iii) $E_{x,45°} = E_{y,45°}$.

Compared to conventional stainless steel, which commonly has a Young's modulus of 200 GPa [32], the studied WAAM material exhibits lower moduli in the $\theta = 0°$ and $\theta = 90°$ cases and a higher modulus in the $\theta = 45°$ case. As discussed in Section 2.3.2, owing to the effect of the geometric undulations, the as-built coupons exhibit lower effective Young's moduli than the machined coupons.

Table 4 Average effective elastic constants of the as-built 3.5 mm coupons.

θ (°)	$E_{x,eff}$ (GPa)	$E_{y,eff}$ (GPa)	$\nu_{xy,eff}$ ( )	$\bar{\nu}_{xy,eff}$ ( )	$G_{xy,eff}$ (GPa)
0	135.9	90.2	0.382	0.398	122.1
45	192.6	192.6	0.025	0.025	41.1
90	90.2	135.9	0.280	0.264	122.1

Table 5 Average effective elastic constants of the as-built 8.0 mm coupons.

θ (°)	$E_{x,eff}$ (GPa)	$E_{y,eff}$ (GPa)	$\nu_{xy,eff}$ ( )	$\bar{\nu}_{xy,eff}$ ( )	$G_{xy,eff}$ (GPa)
0	137.1	109.1	0.451	0.423	104.2
45	201.2	201.2	0.076	0.076	44.2
90	109.1	137.1	0.306	0.336	104.2

Table 6 Average elastic constants of the machined coupons.

| θ (°)	E_x (GPa)	E_y (GPa)	ν_{xy} ( )	$\bar{\nu}_{xy}$ ( )	G_{xy} (GPa)
0	143.3	139.6	0.423	0.418	100.8
45	219.5	219.5	0.108	0.108	50.0
90	139.6	143.3	0.403	0.408	100.8

3.3.2 Poisson's ratio

In this paper, the Poisson's ratio is taken as the negative relationship between the transverse strains and the longitudinal strains, thus:

$$\nu_{xy} = -\frac{\varepsilon_y}{\varepsilon_x}. \tag{18}$$

In the linear elastic range of the material behaviour, similar values were obtained for the 'secant' Poisson's ratio, as defined in Equation (18), and the 'tangent' Poisson's ratio given by $\nu_{xy} = -d\varepsilon_y / d\varepsilon_x$ averaged over the stress range for which the response remained linear, where $d\varepsilon_y$ and $d\varepsilon_x$ are the incremental changes in transverse and longitudinal strains, respectively.

For isotropic materials, the Poisson's ratio must satisfy $-1<\nu_{xy}<0.5$; negative Poisson's ratios indicate 'auxetic' [29, 30] materials, which exhibit transverse expansion under axial tension, while $\nu_{xy} = 0.5$ indicates incompressible materials, such as liquids. For metals, Poisson's ratios typically range between 0.25 and 0.35; for steel [31] and stainless steel [32], ν_{xy} is commonly taken as 0.3. In anisotropic materials, however, Poisson's ratio values are not restricted in this way [33]. Hence, it is not uncommon for anisotropic materials, e.g. composites, to exhibit Poisson's ratios greater than unity [34, 35]. Theoretically, Poisson's ratios in anisotropic materials have no bounds [36].
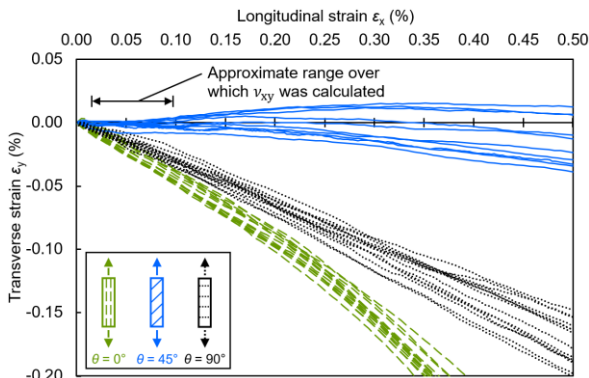
Figure 12 Initial range of the ε_x–ε_y responses for the as-built coupons.
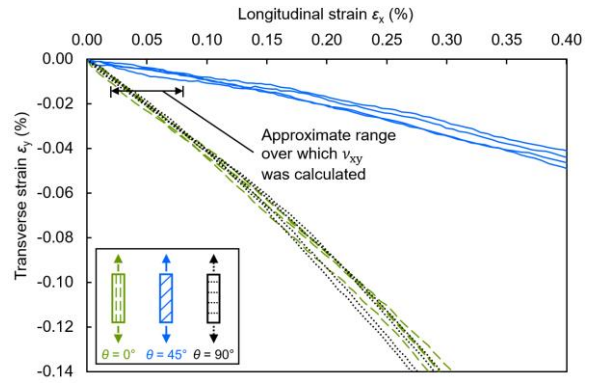
Figure 13 Initial range of the ε_x–ε_y responses for the machined coupons.

In the present study, the elastic constants for the WAAM sheet material have been determined within the linear elastic range $0.1 \leq \sigma/\sigma_{0.2} \leq 0.3$, as indicated approximately in Figures 7(b), 8(b), 12 and 13. For each coupon, a moving median filter with a span of 15 data points was applied to the Poisson's ratio data and subsequently an average was taken within the chosen range. Subsequently, for each angle θ, the average Poisson's ratio between all coupons was calculated. To enforce Equation (1) and thus fulfil the symmetry of the compliance matrix **S** in Equation (2), the following relative optimisation procedure was also conducted:

$$\begin{cases} \min_{\nu_{12},\nu_{21}} \dfrac{(\bar{\nu}_{xy}-\nu_{xy})^2}{\bar{\nu}_{xy}} + \dfrac{(\bar{\nu}_{yx}-\nu_{yx})^2}{\bar{\nu}_{yx}} \\ s.t.\ \bar{\nu}_{yx}E_x = \bar{\nu}_{xy}E_y \end{cases}, \tag{19}$$

where ν_{xy} and ν_{yx} are the average Poisson's ratios measured in the tests, and $\bar{\nu}_{xy}$ and $\bar{\nu}_{yx}$ are the optimised Poisson's ratios. It has been assumed that: (i) For the $\theta = 0°$ cases, $\nu_{xy} = \nu_{xy,0°}$ and $\nu_{yx} = \nu_{xy,90°}$, and vice versa for the $\theta = 90°$ cases; (ii) For the $\theta = 0°$ cases, $E_x = E_{x,0°}$ and $E_y = E_{x,90°}$ and vice versa for the $\theta = 90°$ cases. Assuming that the $\theta = -45°$ and $\theta = 45°$ cases behave in the same manner (i.e. $E_{x,45°} = E_{y,45°}$), the optimisation process resulted in no changes in the $\theta = 45°$ values. Hence, with Figure 10 in mind, the following hold: (i) $\bar{\nu}_{xy,0°} = \nu_{12}$, (ii) $\bar{\nu}_{xy,90°} = \nu_{21}$ and (iii) $\bar{\nu}_{xy,45°} = \bar{\nu}_{yx,45°} = \nu_{xy,45°}$. A similar optimisation procedure has been followed by Bruggi et al. (2021).

As indicated by the machined coupon results in Table 6, the underlying WAAM material has similar Poisson's ratios when tested in the $\theta = 0°$ and $\theta = 90°$ directions and a Poisson's ratio approximately equal to 0.1 when tested in the $\theta = 45°$ direction. Comparing the machined with the as-built coupon results in Tables 4–5, it is observed that the geometric undulations decrease the effective Poisson's ratio in the $\theta = 90°$ case. In the $\theta = 45°$ coupons, the effective Poisson's ratio is close to zero; $\nu \approx 0$ can be found in cellular structures, e.g. honeycombs [38] and cork [33], which exhibit negligible transverse strains when loaded longitudinally.

There are currently very limited investigations on the Poisson's ratio of WAAM stainless steel. Based on tensile tests on three machined $\theta = 0°$ coupons, Al-Nabulsi et al. (2020) reported an average Poisson's ratio of 0.3, matching the value typically used for conventional steel. Bruggi et al. (2021) reported Poisson's ratios of 0.46 ± 0.07 and 0.38 ± 0.04 for machined $\theta = 0°$ and $\theta = 90°$ coupons, respectively, which are similar to those reported herein.

3.3.3 Shear modulus

To determine the shear moduli, the average Young's moduli and average Poisson's ratios, as listed in Tables 4–6, were utilised. Firstly, the shear modulus with respect to the principal material coordinate system G_{12} was calculated using Equation (11), where, $E_1 = E_{x,0°}$, $E_2 =$

$E_{x,90°}$ and $\nu_{12} = \bar{\nu}_{xy,0°}$; the resulting shear modulus is G_{12} = 100.8 GPa for the machined coupons and $G_{12,eff}$ = 122.1 GPa and $G_{12,eff}$ = 104.2 GPa for the as-built 3.5 mm and 8.0 mm coupons, respectively. Subsequently, using G_{12}, for each angle $\theta = \{0°, 45°, 90°\}$, the shear modulus with respect to the Cartesian coordinate system G_{xy} was determined using Equation (9).

The obtained shear moduli are listed in Tables 4–6, where it is observed that, in contrast to the Young's moduli, the shear modulus is lowest in the θ = 45° case. Specifically, $G_{xy,45°}$ is 66%, 58% and 50% lower than $G_{xy,0°} = G_{xy,90°}$ in the case of the as-built 3.5 mm, as-built 8.0 mm and machined coupons, respectively. Compared to conventional stainless steel, which is assumed to have a constant shear modulus of 76.9 GPa [32], the studied WAAM material demonstrates higher shear moduli in the θ = 0° and θ = 90° cases. Conversely, in the θ = 45° case, the studied WAAM material has a much lower shear modulus.

3.4 Variation of elastic constants with direction

In the current section, the average test results, listed in Tables 4–6, are used in conjunction with Equations (6)–(9) and (12) to plot the theoretical variations of the anisotropic elastic constants and shear–extension coupling coefficient, respectively, with the off-axis angle θ (i.e. the direction of loading relative to the deposition direction). Note that the variations shown in Figures 14-18 for the range $0° \leq \theta \leq 90°$ are symmetric with respect to all other quadrants, i.e. $90° \leq \theta \leq 180°$ etc. For comparison, the Young's modulus E, Poisson's ratio ν and shear modulus G of conventional stainless steel are shown in dotted lines.

The theoretical curves for the as-built 3.5 mm, as-built 8.0 mm and machined coupons are shown in Figures 14–16, respectively, alongside the average test results for E_x and $\bar{\nu}_{xy}$ (markers). The test results act as anchor points to the theoretical curves at θ =0° and θ = 90° since they feature directly in Equations (6)–(9).

As shown in Figure 16, since in the machined coupons $E_x \approx E_y$, the variations of the elastic constants with θ are almost symmetrical about the angle θ = 45°, close to which the maximum Young's moduli are $E_{x,44°} = E_{y,46°}$ = 219.5 GPa, the minimum Poisson's ratio is $\nu_{xy,45°}$ = 0.089 and the minimum shear modulus is $G_{xy,45°}$ = 50.0 GPa. As shown in Figures 14–15, since in the as-built coupons there is a bigger difference between $E_{x,eff}$ and $E_{y,eff}$, the variations of the elastic constants (except from $G_{xy,eff}$) with θ are non-symmetric. For the as-built 3.5 mm coupons, the maximum effective Young's moduli are $E_{x,eff,38°} = E_{y,eff,52°}$ = 200.9 GPa, the minimum effective Poisson's ratio is $\nu_{xy,eff,44°}$ = −0.213 and the minimum effective shear modulus is $G_{xy,eff,45°}$ = 41.1 GPa. For the 8.0 mm coupons, the maximum effective Young's moduli are $E_{x,eff,41°} = E_{y,eff,49°}$ = 203.9 GPa, the minimum effective Poisson's ratio is $\nu_{xy,eff,45°}$ = −0.035 and the minimum effective shear modulus is $G_{xy,eff,45°}$ = 44.2 GPa.

The effect of the geometric undulations on the Young's and shear moduli with angle θ is evident in Figure 17. Considering that the magnitudes of geometric undulations relative to the coupon thickness are higher in the 3.5 mm than the 8.0 mm as-built material [20], as geometric variability increases, the effective Young's modulus of WAAM material decreases. The same holds for the shear modulus within approximately the range $15° \leq \theta \leq 75°$; outside this range, as geometric variability increases, the shear modulus also increases. Furthermore, the influence of the undulations on the effective Young's modulus becomes stronger with increasing angle θ as the loading transitions from parallel to the undulations at θ = 0° to perpendicular to the undulations at θ = 90°.

The variations of the shear–extension coupling coefficient $\eta_{xy,x}$ and Poisson's ratio ν_{xy} with respect to θ are shown in Figure 18. By definition, at θ = 0° and θ = 90°, since the material is loaded along its principal axes, $\eta_{xy,x}$ = 0; at the same angles, the Poisson's ratios reach their peak values. For intermediate angles, $\eta_{xy,x}$ achieves similar magnitudes to ν_{xy}. Since $E_{x,0°} \approx E_{x,90°}$, in the case of the machined θ = 45° coupons, $\eta_{xy,x}$ is equal to 0.02 (i.e. 2%), indicating that theoretically predominantly normal strains (and minimal shear strains) were induced in those tests. Therefore, it can be concluded that for the machined $\theta = \{0°, 45°, 90°\}$ cases the measured Young's modulus is also the true Young's modulus of the material.

Further investigation is required on the effect of the shear–extension coupling on the elastic constants of the as-built material. As shown in Figure 18, in the case of the as-built θ = 45° coupons, shear strains of the order of 36% and 19% of the normal strains were induced under the applied longitudinal stress. Preliminary results indicate that this coupling effect leads to differences between the measured and true Young's moduli of the order of 3% in the as-built $\theta = \{0°, 45°, 90°\}$ cases; however more significant differences can potentially occur for other material orientations. Furthermore, as shown in Figures 14 and 15, the agreement between the Poisson's ratios measured in the as-built θ = 45° coupons and the theoretical curves is not as close as in the case of the machined θ = 45° coupons, as shown in Figure 16. This can also be attributed to the coupling effect present in the as-built θ = 45° coupons; i.e. owing to the interaction between shear and normal strains, the measured effective Poisson's ratios $\nu_{xy,eff,45°}$ are not the 'true' Poisson's ratios, but rather the 'apparent' [44] effective Poisson's ratios of the material.
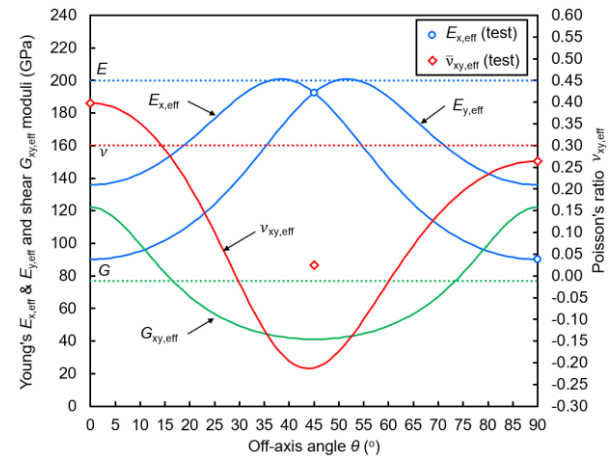

Figure 14 Variation of elastic constants with θ in the as-built 3.5 mm coupons. The dotted lines indicate the typical properties of conventional stainless steel.

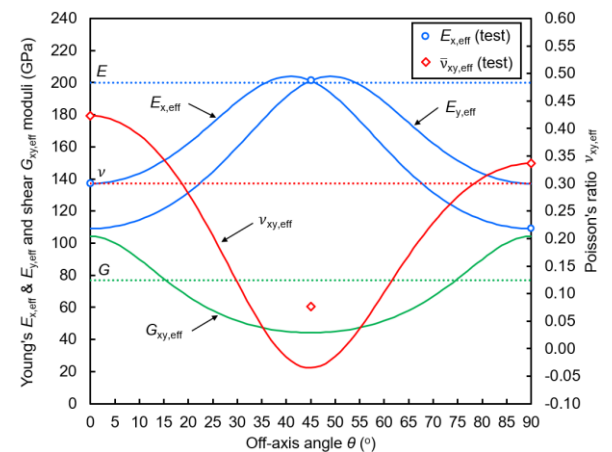**Figure 15** Variation of elastic constants with θ in the as-built 8.0 mm coupons. The dotted lines indicate the typical properties of conventional stainless steel.
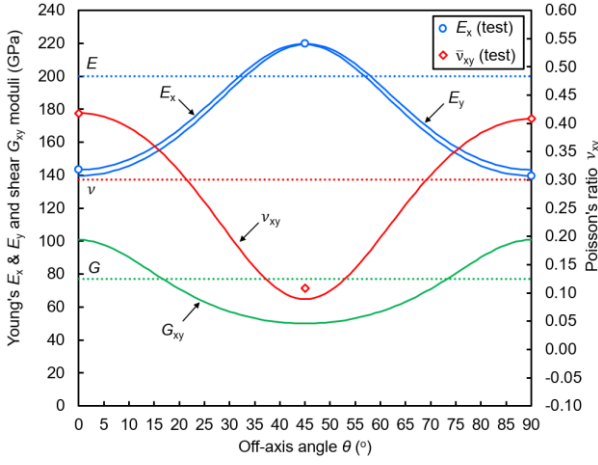
Figure 16 Variation of elastic constants with θ in the machined coupons. The dotted lines indicate the typical properties of conventional stainless steel.
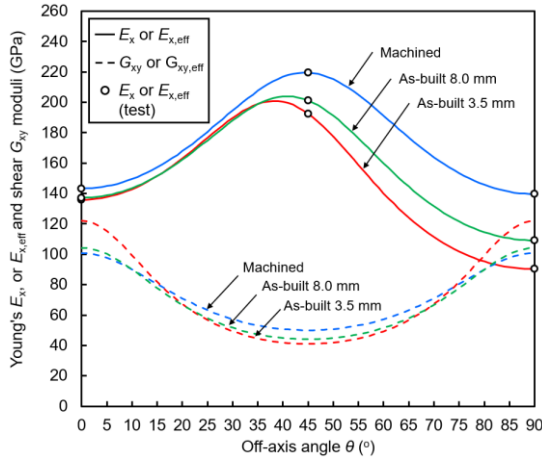

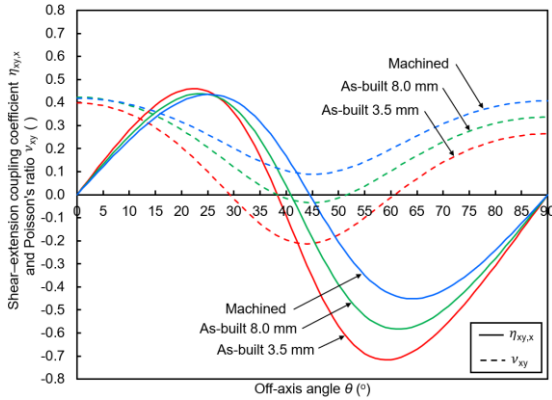**Figure 17** Variation of Young's and shear moduli with θ in all coupons sets.

Figure 18 Variation of the shear–extension coupling coefficient and Poisson's ratio with θ in all coupons sets.

4 Inelastic mechanical response

4.1 Adopted material model and theoretical basis

The classical Hill's yield criterion [40], which is an extension of the von Mises criterion for isotropic materials [41], is adopted herein to describe the anisotropic yielding of the studied WAAM material. For plane stress conditions, the quadratic Hill's yield criterion [41] is:

$$(F\sigma_2{}^2 + G\sigma_1{}^2 + H(\sigma_1 - \sigma_2)^2 + 2N\tau_{12}^2)^{0.5} = \sigma^0 \ , \tag{21}$$

where σ_1, σ_2 and τ_{12} are the normal and shear stresses with respect

to the principal material axes, as defined in Section 3.2, and σ^0 is the reference yield stress. The constants F, G, H and N are given by:

$$F = \frac{1}{2}\left(\frac{1}{R_{22}^2} + \frac{1}{R_{33}^2} - \frac{1}{R_{11}^2}\right) , \tag{22}$$

$$G = \frac{1}{2}\left(\frac{1}{R_{33}^2} + \frac{1}{R_{11}^2} - \frac{1}{R_{22}^2}\right) , \tag{23}$$

$$H = \frac{1}{2}\left(\frac{1}{R_{11}^2} + \frac{1}{R_{22}^2} - \frac{1}{R_{33}^2}\right) , \tag{24}$$

$$N = \frac{3}{2}\frac{1}{R_{12}^2} , \tag{25}$$

while the anisotropic yield stress ratios R_{11}, R_{22}, R_{33} and R_{12} can be obtained using:

$$R_{11} = \frac{\bar{\sigma}_{11}}{\sigma^0}, \ R_{22} = \frac{\bar{\sigma}_{22}}{\sigma^0}, \ R_{33} = \frac{\bar{\sigma}_{33}}{\sigma^0}, \ R_{12} = \frac{\bar{\tau}_{12}}{\tau^0}, \tag{26}$$

where $\tau^0 = \sigma^0/\sqrt{3}$ is the reference yield stress in shear and $\bar{\sigma}_{11}, \bar{\sigma}_{22}$ and $\bar{\sigma}_{33}$ are the yield stresses measured from uniaxial tensile tests in the 1–, 2– and 3–directions, respectively; all 'R-values' must be positive.

For uniaxial off-axis loading, where the applied tensile stress σ_x is applied at angle θ with respect to principal 1–direction, the stress transformations can be conducted using:

$$\begin{bmatrix} \sigma_x \\ \sigma_y \\ \tau_{xy} \end{bmatrix} = \mathbf{T}^{-1} \begin{bmatrix} \sigma_1 \\ \sigma_2 \\ \tau_{12} \end{bmatrix} . \tag{27}$$

Hence, since from Equation (27):

$$\sigma_1 = \sigma_x c^2 \ , \sigma_2 = \sigma_x s^2 \text{ and } \tau_{12} = -\sigma_x sc \ , \tag{28}$$

when uniaxial stress is applied at an angle $\theta = 45°$ relative to the direction of the reference yield stress, at the yield point $\sigma_x = \bar{\sigma}^{45°}$ and therefore $\sigma_1 = \sigma_2 = \tau_{12} = \frac{\sigma_x}{2} = \frac{\bar{\sigma}^{45°}}{2}$; thus, utilising Equations (21)–(23) and (25) leads to:

$$R_{12} = \frac{1}{\left[\frac{4}{3}\left(\frac{\sigma^0}{\bar{\sigma}^{45°}}\right)^2 - \frac{1}{3}\left(\frac{1}{R_{33}}\right)^2\right]^{0.5}} . \tag{29}$$

A similar approach for the determination of R_{12} was employed by Becque (2008).

4.2 Anisotropic yielding in WAAM material

In the current work, $\theta = 0°$ is assumed to be the reference direction, i.e. $\sigma^0 = \bar{\sigma}_{11} = \sigma_{0.2,0°}$, $\bar{\sigma}_{22} = \sigma_{0.2,90°}$ and $\bar{\sigma}^{45°} = \sigma_{0.2,45°}$. Assuming $\bar{\sigma}_{33} = \bar{\sigma}_{11} = \sigma_{0.2,0°}$ [47], the following R-values are thus obtained:

$$R_{11} = 1, \ R_{22} = \frac{\sigma_{0.2,90°}}{\sigma_{0.2,0°}}, \ R_{33} = 1, \ R_{12} = \frac{1}{\left[\frac{4}{3}\left(\frac{\sigma_{0.2,0°}}{\sigma_{0.2,45°}}\right)^2 - \frac{1}{3}\right]^{0.5}} . \tag{30}$$

Utilising the average 0.2% proof stresses listed in Tables 1–3 leads to the R-values listed in Table 7, which can be used to define the anisotropic yielding of WAAM material in ABAQUS [28] using the built-in Hill's criterion feature. This can be achieved using the *PLASTIC command, which defines the general form of the plastic part of the $\sigma-\varepsilon$ response in terms of true stresses and logarithmic plastic strains, and the *POTENTIAL command, which utilises the R-values to adjust the stress values of the inputted $\sigma-\varepsilon$ response and thus accounts for anisotropic yielding. For plane stress models, R_{23} and R_{13} (not defined herein but required in ABAQUS) can be set equal to unity. Note that although the 0.2% proof stresses are used

in the calibration of the R-values, plasticity in fact initiates in stainless steels at far lower stress levels; this can be reflected by using the calculated R-values in conjunction with the widely adopted two-stage Ramberg-Osgood equation [48].

Table 7 Average calculated *R*-values taking $\theta = 0°$ as the reference direction.

Coupon type:	R_{11} ( )	R_{22} ( )	R_{33} ( )	R_{12} ( )
As-built 3.5 mm	1	0.784	1	1.045
As-built 8.0 mm	1	0.834	1	1.111
Machined	1	0.949	1	1.207

5   Conclusions

Wire and arc additively manufactured sheet material demonstrates a degree of anisotropy which is inherent to the manufacturing process. Using experimental data from tensile coupon tests on as-built and machined WAAM stainless steel sheet material, a study has been conducted to establish a modelling approach that can capture the anisotropic material response in both the elastic and inelastic ranges. The tensile coupons were loaded in three different directions (at angles $\theta = \{0°, 45°, 90°\}$) relative to the deposition direction.

In the elastic range, an orthotropic plane stress model has been employed, utilising four elastic constants, namely two Young's moduli, the Poisson's ratio and the shear modulus. The machined WAAM coupons exhibited Young's moduli in the $\theta = 0°$ and $\theta = 90°$ directions that were approximately 30% lower than conventionally produced stainless steel. In the $\theta = 45°$ direction the Young's modulus of the WAAM material was about 10% higher than conventionally produced material. The as-built coupons displayed lower effective Young's moduli than the machined coupons owing to the effect of the geometric undulations. This weakening effect becomes more significant as the loading transitions from parallel to the undulations ($\theta = 0°$) to perpendicular to the undulations ($\theta = 90°$).

Similar values were established for the Poisson's ratio when $\theta = 0°$ and $\theta = 90°$, while a Poisson's ratio of approximately zero was found for $\theta = 45°$. It has been shown that the shear modulus can be obtained by means of off-axis testing, where the material is loaded in tension at an angle θ relative to its principal axes. Compared to conventional stainless steel, both the as-built and machined material achieved a higher shear modulus for $\theta = 0°$ and $\theta = 90°$; conversely, a lower value was achieved for $\theta = 45°$. Overall, the experimental results closely matched the theoretical predictions based on the orthotropic plane stress material model.

Finally, to describe the inelastic response of the WAAM sheet material, the well-known Hill's criterion was utilised. The adopted model requires the material yield stress in three different directions relative to the yield stress in the chosen reference direction.

Acknowledgements

References

[1]   Gao, W.; Zhang, Y.; Ramanujan, D.; Ramani, K.; Chen, Y.; Williams, C.B.; Wang, C.C.L.; Shin, Y.C.; Zhang, S.; Zavattieri, P.D. (2015) *The status, challenges, and future of additive manufacturing in engineering.* Computer Aided Design **69**, 65–89.

[2]   Wu, P.; Wang, J.; Wang, X. (2016) *A critical review of the use of 3-D printing in the construction industry.* Automation in Construction **68**, 21–31.

[3]   Calignano, F.; Manfredi, D.; Ambrosio, E.P.; Biamino, S.; Lombardi, M.; Atzeni, E.; Salmi, A.; Minetola, P.; Iuliano, L.; Fino, P. (2017) *Overview on additive manufacturing technologies.* Proceedings of the Institute of Electrical and Electronics Engineers **105**, 593–612.

[4]   Wu, B.; Myant, C.; Weider, S. (2017) *The value of additive manufacturing: future opportunities.* Institute for Molecular Science and Engineering Imperial College London.

[5]   Labonnote, N.; Rønnquist, A.; Manum, B.; Rüther, P. (2016) *Additive construction: State-of-the-art, challenges and opportunities.* Automation in Construction **72**, 347–366.

[6]   Camacho, D.D.; Clayton, P.; O'Brien, W.J.; Seepersad, C.; Juenger, M.; Ferron, R.; Salamone, S. (2018) *Applications of additive manufacturing in the construction industry – A forward-looking review.* Automation in Construction **89**, 110–119.

[7]   Buchanan, C.; Gardner, L. (2019) *Metal 3D printing in construction: A review of methods, research, applications, opportunities and challenges.* Engineering Structures **180**, 332–348.

[8]   Williams, S.W.; Martina, F.; Addison, A.C.; Ding, J.; Pardal, G.; Colegrove, P. (2016) *Wire + Arc additive manufacturing.* Materials Science and Technology **32**, 641–647.

[9]   Gardner, L.; Kyvelou, P.; Herbert, G.; Buchanan, C. (2020) *Testing and initial verification of the world's first metal 3D printed bridge.* Journal of Constructional Steel Research **172**, 106233.

[10]   Lange, J.; Feucht, T.; Erven, M. (2020) *3D printing with steel: Additive Manufacturing for connections and structures.* Steel Construction **13**, 144–153.

[11]   MX3D (2020) *MX3D Robot Arm.* https://mx3d.com/projects/robot-arm/ (accessed 21.01.2021).

[12]   National Institute of Standards and Technology (2013) *Measurement Science Roadmap for Metal-Based Additive Manufacturing.* National Institute of Standards and Technology, U.S. Department of Commerce.

[13]   Luecke, W.E.; Slotwinski, J.A. (2014) *Mechanical properties of austenitic stainless steel made by additive manufacturing.* Journal of Research of the National Institute of Standards and Technology **119**, 398–418.

[14]   Le, V.T.; Mai, D.S.; Hoang, Q.H. (2020) *A study on wire and arc additive manufacturing of low-carbon steel components: process stability, microstructural and mechanical properties.* Journal of the Brazilian Society of Mechanical Sciences and Engineering **42**, 42:480.

[15]   Nemani, A.V.; Ghaffari, M.; Nasiri, A. (2020) *Comparison of microstructural characteristics and mechanical properties of shipbuilding steel plates fabricated by conventional rolling versus wire arc additive manufacturing.* Additive Manufacturing **32**, 101086.

[16]   Gordon, J.V.; Haden, C.V.; Nied, H.F.; Vinci, R.P.; Harlow, D.G.; (2018) *Fatigue crack growth anisotropy, texture and residual stress in austenitic steel made by wire and arc additive manufacturing.* Materials Science and Engineering A **724**, 431–438.

[17] Laghi, V.; Palermo, M.; Tonelli, L.; Gasparini, G.; Ceschini, L.; Trombetti, T. (2020) *Tensile properties and microstructural features of 304L austenitic stainless steel produced by wire-and-arc additive manufacturing*. International Journal of Advanced Manufacturing Technology **106**, 3693–3705.

[18] Wang, L.; Xue, J.; Wang, Q. (2019) *Correlation between arc mode, microstructure, and mechanical properties during wire arc additive manufacturing of 316L stainless steel*. Materials Science and Engineering A **751**, 183–190.

[19] Ji, L.; Lu, J.; Jing, C.; Fan, H.; Ma, S. (2017) *Microstructure and mechanical properties of 304L steel fabricated by arc additive manufacturing*. MATEC Web of Conferences **128**, 03006.

[20] Kyvelou, P.; Slack, H.; Mountanou, D.D.; Wadee, A.M.; Britton, T.B.; Buchanan, C.; Gardner, L. (2020) *Mechanical and microstructural testing of wire and arc additively manufactured sheet material*. Materials and Design **192**, 108675.

[21] Haghdadi, N.; Laleh, M.; Moyle, M.; Primig, S. (2021) *Additive manufacturing of steels: a review of achievements and challenges*. Journal of Materials Science **56**, 64–107.

[22] Laghi, V.; Palermo, M.; Gasparini, G.; Girelli, V.A.; Trombetti, T. (2021) *On the influence of the geometrical irregularities in the mechanical response of Wire-and-Arc Additively Manufactured planar elements*. Journal of Constructional Steel Research **178**, 106490.

[23] Jones, R.M. (1975) *Mechanics of composite materials*. Taylor & Francis, London, UK.

[24] Vasiliev, V.V.; Morozov, E.V. (2001) *Mechanics and Analysis of Composite Materials*. Elsevier Science Ltd, Oxford, UK.

[25] Bruggi, M.; Laghi, V.; Trombetti, T. (2021) *Simultaneous design of the topology and the build orientation of Wire-and-Arc Additively Manufactured structural elements*. Computers and Structures **242**, 106370.

[26] Dodwell, T.J.; Flemming, L.; Buchanan, C.; Kyvelou, P.; Detommaso, G.; Gosling, P.D.; Scheichl, R.; Kendall, W. S.; Gardner, L.; Girolami, M. A.; Oates, C.J. (2021) *Building Bridges: A Data-Centric Approach to Modelling 3D-Printed Steel*. Proceedings of the National Academy of Sciences of the USA.

[27] Lekhnitskii et al. (1981) *Theory of Elasticity of an Anisotropic Elastic Body*. Mir Publishers, Moscow.

[28] Abaqus (2014). *Abaqus analysis user's guide : Online documentation. Version 6.14-2*. Providence, RI: Dassault Systèmes Simulia Corp.

[29] Evans, K.E.; Nkansah, M.A. (1991) *Molecular network design*. Nature **353**(6340), 124.

[30] Wadee, A.M.; Phillips, A.T.M.; Bekele, A. (2020) *Effects of Disruptive Inclusions in Sandwich Core Lattices to Enhance Energy Absorbency and Structural Isolation Performance*. Frontiers in Materials **7**:134.

[31] EN 1993-1-1. (2005) *Eurocode 3: Design of Steel Structures – Part 1-1: General rules and rules for buildings*. European Committee for Standardization (CEN), Brussels, Belgium.

[32] SCI P413. (2017) *Design manual for structural stainless steel. 4ᵗʰ ed.* The Steel Construction Institute. Ascot, UK.

[33] Greaves, G.N.; Greer, A.L.; Lakes, R.S.; Rouxel, T. (2011) *Poisson's ratio and modern materials*. Nature Materials **10**, 823–837.

[34] Lempriere, B.M. (1968) *Poisson's ratio in orthotropic materials*. AIAA Journal **6**, 2226–2227.

[35] Lethbridge Z.A.D; Walton, R.I.; Marmier, A.S.H.; Smith, C.W.; Evans, K.E. (2010) *Elastic anisotropy and extreme Poisson's ratios in single crystals*. Acta Materialia **58**, 6444–6451.

[36] Ting, T.; Chen, T. (2005) *Poisson's ratio for anisotropic elastic materials can have no bounds*. Quarterly Journal of Mechanics and Applied Mathematics **58**(1), 73–82.

[37] Dowling N. (2013) *Mechanical behavior of materials: engineering methods for deformation, fracture, and fatigue, 4th ed.* Pearson Education Ltd, Essex, UK.

[38] Grima, J.N.; Oliveri, L.; Attard, D.; Ellul, B.; Gatt, R.; Cicala, G.; Recca, G. (2010) *Hexagonal honeycombs with zero Poisson's ratios and enhanced stiffness*. Advanced Engineering Materials **12**(9), 855–862.

[39] Al-Nabulsi, Z.; Mottram, J.T.; Gillie, M.; Kourra, N.; Williams, M.A. (2020) *Mechanical and X-ray computed tomography characterisation of a WAAM 3D printed steel plate for structural engineering applications*. Construction and Building Materials, 121700.

[40] Hill, R. (1948) *A theory of the yielding and plastic flow of anisotropic metals*. Proceedings of the Royal Society of London. Series A. Mathematical and Physical Sciences **193**, 281–297.

[41] Mises, R. (1928) *Mechanik der plastischen Formänderung von Kristallen*. ZAMM-Journal of Applied Mathematics and Mechanics/Zeitschrift für Angewandte Mathematik und Mechanik **8**, 161–185.

[42] Becque, J. (2008) *The Interaction of Local and Overall Buckling of Cold-Formed Stainless Steel Columns*. PhD Thesis, The University of Sydney.

[43] Vanucci, P. (2018) *Anisotropic elasticity. Lecture notes in applied and computational mechanics*, *Volume 85*. Springer, Singapore.

[44] Morozov, E.V.; Vasiliev, V.V. (2003) *Determination of the shear modulus of orthotropic materials from off-axis tension tests*. Composite Structures **62**, 379–382.

[45] EN ISO 6892-1. (2016) *Metallic Materials - Tensile Testing – Part 1: Method of Test at Room Temperature*, European Committee for Standardization (CEN), Brussels, Belgium.

[46] LaVision, *DaVis* (Version 8.4.0) [Software] La Vision GmbH, 2017.

[47] Rasmussen, K.J.R.; Burns, T.; Bezkorovainy, P.; Bambach, M.R. (2003) *Numerical modelling of stainless steel plates in compression*. Journal of Constructional Steel Research **59**, 1345–1362.

[48] Arrayago, I.; Real, E.; Gardner, L. (2015) *Description of stress-strain curves for stainless steel alloys*. Materials & Design **87**, 540–55.